

## ChemComm

## Tunable Synthesis of Magnetoelectric CoFe2O4- BaTiO3 Core-Shell Nanowires

Journal:	ChemComm
Manuscript ID	CC-COM-07-2024-003701.R2
Article Type:	Communication

SCHOLARONE™ Manuscripts

### ChemComm

## COMMUNICATION

# Tunable Synthesis of Magnetoelectric CoFe<sub>2</sub>O<sub>4</sub>- BaTiO<sub>3</sub> Core-Shell Nanowires

Noah D. Ferson<sup>a</sup>, John R. Ganiban<sup>a</sup>, David P. Arnold<sup>b</sup>, and Jennifer S. Andrew<sup>a</sup>

Received 00th January 20xx, Accepted 00th January 20xx

DOI: 10.1039/x0xx00000x

A template-assisted synthesis approach was employed to tune the structure and properties of  $CoFe_2O_4$ -BaTiO $_3$  core-shell magnetoelectric nanowires. By adjusting the composition of the nanowires, we achieved control over the magnetic anisotropy in the  $CoFe_2O_4$  core phase. This work highlights the potential for enhanced magnetic anisotropy to improve magnetoelectric performance.

Multiferroics are a class of multifunctional materials that combine at least two ferroic ordering parameters, e.g., ferroelectric, ferromagnetic, and ferroelastic. The ferroic orderings, along with their respective properties of polarization, magnetization, and strain, are well suited for use in collective state switches, resulting in significant interest in multiferroics for novel memory and logic devices.<sup>1–4</sup> In these applications, device scalability is crucial for continued enhancements in memory and compute density. Nanostructured multiferroics offer particular advantages in these applications, where, compared to their bulk counterparts, they are expected to exhibit enhanced magnetoelectric coupling coefficients and demonstrate superior scalability.<sup>1,5–8</sup>

A key property of multiferroic materials is their magnetoelectric (ME) coupling, which enables the voltage control of magnetism, and vice versa. Composite ME materials, where a piezoelectric is strain-coupled with a magnetostrictive material, overcome limitations attributed to single-phase ME multiferroics (e.g., ordering temperatures well below room temperature).<sup>9</sup> In a nanostructured ME composite, the interfacial area between the magnetostrictive and piezoelectric phases is maximized, facilitating greater strain transfer and enhanced coupling.<sup>9</sup> Moreover, high aspect ratio nanostructures, such as nanowires, offer a method to

investigate the effects of anisotropy on the resulting ME properties.  $^{7,10,11}$  In this work, we specifically investigate the contribution of magnetic anisotropy and its tunability by controlling the relative fractions of the core and shell phases in magnetoelectric CoFe<sub>2</sub>O<sub>4</sub>-BaTiO<sub>3</sub> core-shell nanowires.

Core-shell nanowires have previously been fabricated using several techniques, including coaxial electrospinning, 12,13 template-assisted methods, 14 and solvo-/hydro- thermal processes. 15,16 Among these, template-assisted approaches are particularly promising and can be applied in conjunction with sol-gel processing and electrochemical techniques for the fabrication of high quality nanocomposites with tailored compositions. While core-shell magnetoelectric nanowires have been previously synthesized using template-assisted methods, 14,17 the effect of varying the fraction of the core and shell phases on their properties has rarely been studied. Here, demonstrate that compositional variance magnetoelectric CoFe<sub>2</sub>O<sub>4</sub>-BaTiO<sub>3</sub> nanowires can be varied using synthetic procedures to generate ME nanowires with tunable magnetic anisotropy and ME coupling.

Magnetoelectric core-shell nanowires were fabricated in an anodic aluminum oxide (AAO) template, where BaTiO<sub>3</sub> shells were first fabricated, followed by electrodeposition and oxidation of CoFe<sub>2</sub> to form CoFe<sub>2</sub>O<sub>4</sub>-BaTiO<sub>3</sub> core-shell nanowires. An overview of the process is presented in Fig. 1a (a complete description of the core-shell nanowire synthesis and within the characterization is included electronic supplementary information (ESI)). Briefly, AAO templates were coated with an amorphous BaTiO<sub>3</sub> gel via a vacuum-assisted solgel template wetting process. The thickness of the BaTiO<sub>3</sub> gel can be increased by repeating the template wetting process multiple times. The amorphous BaTiO<sub>3</sub> gel was then crystallized by calcination at 650 °C for 6 hours. Fig. 1b shows that the BaTiO<sub>3</sub> yield increases and then plateaus after three wetting

<sup>&</sup>lt;sup>a.</sup> Dept. of Materials Science & Engineering, University of Florida, Gainesville, FL 32611, USA.

b. Dept. of Electrical & Computer Engineering, University of Florida, Gainesville, FL 32611, USA.

<sup>†</sup> Footnotes relating to the title and/or authors should appear here. Electronic Supplementary Information (ESI) available: [details of any supplementary information available should be included here]. See DOI: 10.1039/x0xx00000x

COMMUNICATION ChemComm

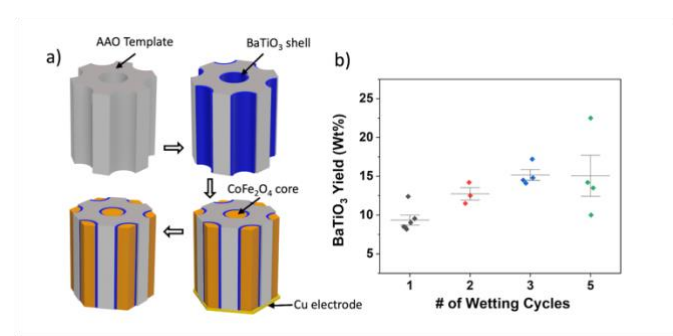


**Fig. 1** (a) Schematic of porous anodic aluminium oxide (AAO) template based CoFe<sub>2</sub>O<sub>4</sub>-BaTiO<sub>3</sub> core-shell nanowire synthesis with open arrows indicating synthesis path and (b) BaTiO<sub>3</sub> nanotube yield in AAO templates after calcination with respect to the number of wetting cycles used during synthesis.

cycles, demonstrating the ability to tune  $BaTiO_3$  yield via increasing the number of wetting cycles. The plateau in yield for samples prepared with more than three wetting cycles is attributed to the decreasing sol-gel stability, as the solution continues to undergo hydrolysis and condensation reactions due to the extended time required for template wetting. This limitation could potentially be addressed by developing a more stable  $BaTiO_3$  sol-gel solution, possibly by the addition of chelating agents.

To complete the core-shell nanowire synthesis, a  $CoFe_2$  core was deposited via electrochemical deposition into the  $BaTiO_3$  shells. The final schematic in Fig. 1a depicts the core-shell nanowires within the AAO template. To generate free-standing nanowires, the AAO template can be preferentially etched using 2 M NaOH to facilitate nanowire release.

X-ray diffractometry (XRD) was performed on free-standing nanowires to confirm the formation of perovskite  $BaTiO_3$  and spinel  $CoFe_2O_4$  (Fig. S1, ESI). Peaks characteristic of tetragonal  $BaTiO_3$  were indexed from the diffraction patterns. However, peak splitting arising from the elongated c-axis in the perovskite structure cannot be distinguished due to the nanocrystalline nature of the  $BaTiO_3$  nanotubes. Consequently, additional phase identification was performed using Raman spectroscopy, which probes intermediate and long range ordering. Modes typical of tetragonal perovskite  $BaTiO_3$  are revealed in Fig. S2 (ESI). For example, the band at ca.  $307 \text{ cm}^{-1}$  is attributed to the  $B_1$  and E(TO + LO) phonon modes, which are characteristic to the polar tetragonal phase of  $BaTiO_3$ .  $^{19,20}$ 

The nanowire morphology was then evaluated using a combination of scanning electron microscopy (SEM), focus ion beam SEM (FIB-SEM), and scanning transmission electron microscopy (STEM). Fig. 2a shows a longitudinal cross-section of the AAO template with embedded core-shell nanowires, while Fig. 2b displays the free-standing core-shell nanowires after chemical etching of the AAO template. A transverse cross section of nanowires in template was prepared using FIB-SEM (Fig. 2c), demonstrating the complete filling of pores. The high angle annular dark field (HAADF) micrograph shown in Fig. 2d reveals the core-shell morphology with a distinct interface between the constituent phases.

Next, vibrating sample magnetometry (VSM) was performed on free-standing nanowires after release from their templates. Mass-magnetization curves are presented in Fig. 3 for samples

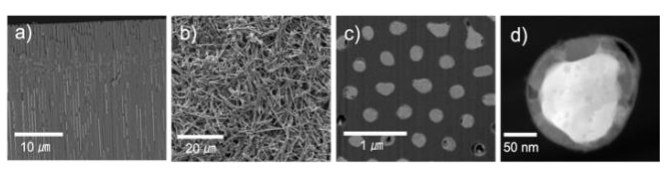


**Fig. 2** (a) Longitudinal cross sectional electron micrograph of core-shell nanowires after deposition into the AAO template, (b) freestanding nanowires after release via chemical etching, (c) FIB transverse cross section of nanowires in AAO, and (d) STEM-HAADF image of a core-shell nanowire cross section.

prepared with zero to three BaTiO<sub>3</sub> wetting cycles. The fraction of  $CoFe_2O_4$  in core-shell nanowires was established by comparing  $CoFe_2O_4$  saturation magnetization (M<sub>s</sub>) to that of  $CoFe_2O_4$  nanowires (M<sub>s</sub> = 16.7 emu g<sup>-1</sup>) prepared with zero BaTiO<sub>3</sub> wetting cycles. Nanowires prepared with one and three wetting cycles contain 88.7, and 74.7 wt.%  $CoFe_2O_4$ , respectively, indicating the composition of the core-shell nanowires can be tuned by increasing the number of BaTiO<sub>3</sub> template wetting cycles. The reduced M<sub>s</sub> of the  $CoFe_2O_4$  nanowires presented here, compared to the bulk value of approximately 80 emu g<sup>-1</sup>, aligns with previous studies for  $CoFe_2O_4$  nanowires heat treated at 600 °C.<sup>21</sup> This reduction has been attributed to their small average crystallite sizes (16.1 nm from Scherrer's analysis, ESI).

Magnetoelectric coupling in core-shell nanowires was investigated by examining their magnetic properties before and after in situ thermal depolarization. Prior to magnetic measurements, the nanowires were electrically poled ex situ via corona poling (a complete description of the experimental details are included within the ESI). Fig. 4a displays a room temperature VSM hysteresis loop for electrically poled coreshell nanowires prepared with three BaTiO<sub>3</sub> wetting cycles before (blue, dashed) and after (orange, solid) thermal depolarization. Upon examining the hysteresis loop, it was observed that the M<sub>s</sub> increased after thermal depolarization. This indicates that the corona poling process initially decreased the M<sub>s</sub> of the CoFe<sub>2</sub>O<sub>4</sub> core as a remnant strain was generated within the BaTiO<sub>3</sub> shell. These results are consistent with previous work investigating magnetoelectric coupling in mesoporous ME composites.22

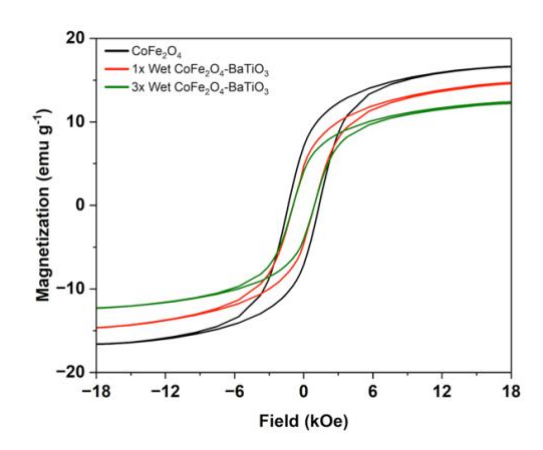


Fig. 3 VSM hysteresis loops for CoFe<sub>2</sub>O<sub>4</sub> nanowires (black) and core-shell nanowires prepared with one (red) and three (green) BaTiO<sub>3</sub> wetting cycles.

**Journal Name** COMMUNICATION

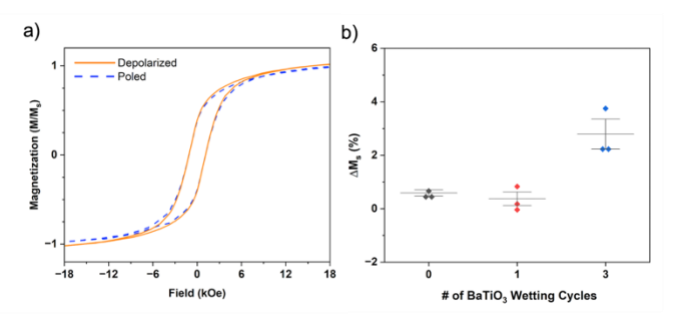


Fig. 4 (a) Magnetization vs field data for ex situ poled nanowires via a corona discharge process (blue) and after in situ thermal depolarization (orange) and (b) compiled change in saturation magnetization ( $\Delta M_s$ ) with respect to the number of BaTiO<sub>3</sub> wetting cycles implemented during synthesis.

The percent change in saturation magnetization ( $\Delta M_s$ ) was quantified for nanowires before (poled) and after (depoled)

thermal depolarization according to eqn. (1). 
$$\Delta M_s = \frac{(M_{s \; Depoled} \; ^- M_{s \; Poled})}{M_{s \; Poled}} \times 100\% \quad (1)$$

In Fig. 4b,  $\Delta M_s$  values are shown with respect to the number of BaTiO₃ wetting cycles implemented during synthesis. Samples prepared with zero (the pure CoFe<sub>2</sub>O<sub>4</sub> control) and one BaTiO<sub>3</sub> wetting cycle exhibit a  $\Delta M_s$  of 0.66  $\pm$  0.21 % and 0.37  $\pm$ 0.44 %, respectively (representative hysteresis loops are presented in Fig S3, ESI). The lack of coupling evident in the sample prepared with one BaTiO<sub>3</sub> wetting cycle may be explained by the diminished mechanical coupling between the core and shell phases as the piezoelectric phase fraction is reduced.<sup>23</sup> However, the core-shell nanowires with the greatest BaTiO<sub>3</sub> fraction (i.e., prepared with three BaTiO<sub>3</sub> wetting cycles) present an average  $\Delta M_s$  of 2.87  $\pm$  0.9 %, which indicates the core and shell phases of the composite nanowires are strain coupled, potentially leading to magnetoelectric coupling.

To further examine the coupling between the core and shell phases, magnetization vs temperature (M vs. T) measurements were performed using superconducting quantum interference device (SQUID) magnetometry. Core-shell nanowires prepared with three BaTiO<sub>3</sub> wetting cycles exhibit a distinct change in magnetization near the orthorhombic to rhombohedral phase transition for BaTiO<sub>3</sub>, indicating the core and shell phases are strain coupled (Fig. S5, ESI). Ultimately, the results presented from the VSM depolarization and SQUID M vs. T investigations provide indirect evidence for the presence of ME coupling, which is prominent with an increased fraction of BaTiO₃ in the core-shell nanowires.

As the thickness of the BaTiO₃ shell increases, it is anticipated that there will be a corresponding increase in the magnetic anisotropy of the CoFe<sub>2</sub>O<sub>4</sub> core. To study this, a magnetic field was applied either parallel or perpendicular to the nanowire long axis while in template during VSM, corresponding to the magnetic easy and hard axes, respectively. The remnant magnetization for samples magnetized along the easy axis  $(M_{r//})$  vs. the hard axis  $(M_{r\perp})$  was evaluated to probe the magnetic texture  $(M_{r//}/M_{r\perp})$  of the nanowires.<sup>24</sup> In Fig. 5a,  $M_{r/\!/}/M_{r\perp}$  values are presented with respect to the nanowire length for CoFe<sub>2</sub>O<sub>4</sub> (blue) and CoFe<sub>2</sub>O<sub>4</sub>-BaTiO<sub>3</sub> (orange) nanowires. The linear fit for the respective data sets is also presented as dashed lines to guide the eye. Fig. 5a reveals that

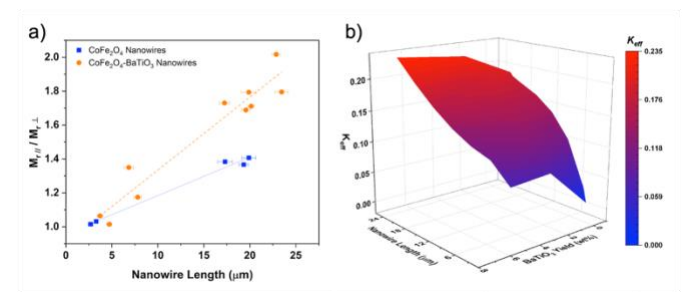


Fig. 5 (a) Magnetic texture  $(M_{r/f}/M_{r\perp})$  as a function of nanowire length for  $CoFe_2O_4$  nanowires (blue square) and core-shell nanowires (orange closed circle), error bars represent the standard deviation for the nanowire lengths. (b) Surface plot of the effective anisotropy constant  $(K_{eff})$  for  $CoFe_2O_4$ -BaTiO<sub>3</sub> nanowires in template as a function of nanowire length and the recorded BaTiO<sub>3</sub> violed during a pathletic process. yield during synthesis.

the value for  $M_{r/\!/}/M_{r\perp}$  increases with nanowire length. Interestingly, for CoFe<sub>2</sub>O<sub>4</sub>-BaTiO<sub>3</sub> nanowires, this effect is more prominent, which could be a result of increased anisotropy compared to that of CoFe<sub>2</sub>O<sub>4</sub> nanowires due to the increasing aspect ratio of the CoFe<sub>2</sub>O<sub>4</sub> core as the BaTiO<sub>3</sub> shell thickness increases. To investigate this effect further, the effective anisotropy constant was evaluated.

In Fig. 5b, the surface plot of the effective anisotropy constant (Keff) as a function of nanowire length and BaTiO<sub>3</sub> yield during the nanowire synthesis is presented. The effect of shape anisotropy is clear, where Keff increases as the nanowire length increases. Yet, Keff also increases with BaTiO<sub>3</sub> yield, and presumably the BaTiO<sub>3</sub> shell thickness. There are two factors that could be influencing Keff: (1) the increasing aspect ratio of the CoFe<sub>2</sub>O<sub>4</sub> core due to increasing BaTiO<sub>3</sub> shell thickness or (2) decreased dipolar interactions between neighboring CoFe<sub>2</sub>O<sub>4</sub> cores as the BaTiO<sub>3</sub> shell thickness increases. Ultimately, these results indicate that the anisotropy induced in the CoFe<sub>2</sub>O<sub>4</sub> core can be tuned by how many BaTiO<sub>3</sub> wetting cycles are implemented during synthesis.

The Keff of the nanowire arrays was calculated as the area between the magnetization curves taken along the easy and hard axes according to eqn. (2).25

$$K_{eff} = \int_0^{M_s} H_{\perp} dM - \int_0^{M_s} H_{//} dM$$
 (2)

To clarify the origin of increasing anisotropy that was revealed in Fig. 5b, the contributions of Keff are presented through a description of the effective anisotropy field (Heff) of the CoFe<sub>2</sub>O<sub>4</sub> core. H<sub>eff</sub> can be evaluated for nanowire arrays with non-negligible magnetocrystalline anisotropy (as is the case for  $CoFe_2O_4$ ) according to eqn. (3).<sup>26,27</sup>

$$H_{eff} = 2\pi M_s - 6\pi M_s P + H_{mc}$$
 (3)

With H<sub>eff</sub> being related to K<sub>eff</sub> according to eqn.(4).<sup>28</sup>  $H_{eff} = \frac{2 \, K_{eff}}{\mu_o M_S} \qquad (4)$ 

$$H_{eff} = \frac{2 K_{eff}}{\mu M_c}$$
 (4)

Where Ms is the saturation magnetization, P is the filling factor, H<sub>mc</sub> is the contribution of the magnetocrystalline anisotropy, and  $\mu_0$  is the vacuum permeability. The first two terms in eqn. (3) are the magnetostatic and dipolar interaction contributions, respectively. In practice, a magnetic material will have a constant Ms and Hmc, and when deposited within a given AAO template, the value of P will also be constant. However, for CoFe<sub>2</sub>O<sub>4</sub>-BaTiO<sub>3</sub> core-shell nanowires, as the BaTiO<sub>3</sub> shell thickness increases, P will decrease and thus the dipolar

COMMUNICATION ChemComm

interaction field will diminish and an increase in  $H_{eff}$  for  $CoFe_2O_4$  will be observed. This explains why  $K_{eff}$  is modulated by both the nanowire length and the thickness of the  $BaTiO_3\,shell$ , or more precisely, the spacing between  $CoFe_2O_4$  cores while in template. This finding supports the notion that the processing conditions chosen can be used to tune the properties of core-shell ME nanowires.

In order to account for the variation in nanowire diameter in the presented analysis, the pore size distribution of the AAO templates was determined. The pore diameter (d<sub>P</sub>) distribution will have direct implications on the magnitude of the filling factor, P, and ultimately, H<sub>eff</sub>. Using ImageJ analysis, the magnitude of d<sub>P</sub> was determined to be 199.6  $\pm$  18.8 nm (Fig. S6, ESI), (further details are presented within the ESI). Due to the narrow size distribution of d<sub>P</sub>, its impact on the analysis is expected to be negligible, with errors being relatively small (< 10%). Therefore, minimal changes in the H<sub>eff</sub> are expected.

In this communication a synthesis approach for core-shell ME nanowires, enabling tunability of the final composition in the nanocomposite, is presented. A range of sample compositions were investigated for  $CoFe_2O_4$ -BaTiO $_3$  nanowires. Notably, anisotropy in the  $CoFe_2O_4$  core increases with BaTiO $_3$  shell thickness due to a combination of increased spacing between the  $CoFe_2O_4$  cores and larger aspect ratios while in the template. Further exploration of sample composition is needed to establish a complete model of the effect of increasing shell thickness on the resulting anisotropy of the magnetic core and ME performance, this could be achieved using templates with varying spacing and pore diameters. Ultimately, this work shows great promise for the synthesis of ME nanowires with tunable anisotropy by a template-assisted process.

This work was supported in part by the National Science Foundation (NSF) I/UCRC on Multi-functional Integrated System Technology (MIST Center) IIP-1939009. This work was partly conducted at the Research Service Centers of the Herbert Wertheim College of Engineering at the University of Florida. The authors would like to thank Professors Julia Glaum and Juan Nino for their insightful discussion during the construction of the corona discharge poling station and Professor Carlos Rinaldi-Ramos and Eric Imhoff for assistance performing SQUID measurements.

### Data availability

The data underlying this study are available in the published article and its electronic supplementary information (ESI).

#### **Conflicts of interest**

There are no conflicts to declare.

### **Notes and references**

1 S. Manipatruni, D. E. Nikonov, C.-C. Lin, T. A. Gosavi, H. Liu, B. Prasad, Y.-L. Huang, E. Bonturim, R. Ramesh and I. A. Young, *Nature*, 2019, **565**, 35–42.

- 2 R. Ramesh and S. Manipatruni, Proc. R. Soc. A., 2021, 477, 20200942.
- 3 J. T. Heron, J. L. Bosse, Q. He, Y. Gao, M. Trassin, L. Ye, J. D. Clarkson, C. Wang, J. Liu, S. Salahuddin, D. C. Ralph, D. G. Schlom, J. Íñiguez, B. D. Huey and R. Ramesh, *Nature*, 2014, 516, 370–373.
- 4 S. Manipatruni, D. E. Nikonov and I. A. Young, *Nature Phys*, 2018, **14**, 338–343.
- S. Hohenberger, V. Lazenka, S. Selle, C. Patzig, K. Temst and M. Lorenz, *Physica Status Solidi (b)*, 2020, 257, 1900613.
- 6 Y. Liu, G. Sreenivasulu, P. Zhou, J. Fu, D. Filippov, W. Zhang, T. Zhou, T. Zhang, P. Shah, M. R. Page, G. Srinivasan, S. Berweger, T. M. Wallis and P. Kabos, *Sci Rep*, 2020, **10**, 20170.
- 7 M. J. Bauer, X. Wen, P. Tiwari, D. P. Arnold and J. S. Andrew, Microsyst Nanoeng, 2018, 4, 37.
- 8 M. J. Bauer, A. Thomas, B. Isenberg, J. Varela, A. Faria and D. P. Arnold, *IEEE SENSORS JOURNAL*, 2020, **20**, 7.
- J. S. Andrew, J. D. Starr and M. A. K. Budi, *Scripta Materialia*, 2014, **74**, 38–43.
- 10 Y. Yan, Y. Zhou and S. Priya, Appl. Phys. Lett., 2013, 102, 052907.
- 11 J. L. Jones, J. D. Starr and J. S. Andrew, *Appl. Phys. Lett.*, 2014, **104**, 242901.
- 12 H. Chen, N. Wang, J. Di, Y. Zhao, Y. Song and L. Jiang, *Langmuir*, 2010, **26**, 11291–11296.
- 13 S. Xie, F. Ma, Y. Liu and J. Li, Nanoscale, 2011, 3, 3152.
- 14 D. Sallagoity, C. Elissalde, J. Majimel, M. Maglione, Vlad. A. Antohe, F. Abreu Araujo, P. M. Pereira de Sá, S. Basov and L. Piraux, *RSC Adv.*, 2016, **6**, 106716–106722.
- S. Mushtaq, K. Shahzad, M. Rizwan, A. Ul-Hamid, B. H. Abbasi,
  W. Khalid, M. Atif, N. Ahmad, Z. Ali and R. Abbasi, *RSC Adv.*,
  2022, 12, 24958–24979.
- 16 Y. Zhang, B. Su, Y. Tian, Z. Yu, X. Wu, J. Ding, C. Wu, D. Wei, H. Yin, J. Sun and H. Fan, *Acta Biomaterialia*, 2023, **168**, 470–483.
- 17 D. Sallagoity, C. Elissalde, J. Majimel, R. Berthelot, U. C. Chung, N. Penin, M. Maglione, V. A. Antohe, G. Hamoir, F. Abreu Araujo and L. Piraux, *J. Mater. Chem. C*, 2015, **3**, 107–111.
- 18 L. R. Prado, N. S. De Resende, R. S. Silva, S. M. S. Egues and G. R. Salazar-Banda, *Chemical Engineering and Processing: Process Intensification*, 2016, **103**, 12–20.
- 19 U. A. Joshi, S. Yoon, S. Baik and J. S. Lee, *J. Phys. Chem. B*, 2006, **110**, 12249–12256.
- 20 T.-C. Huang, M.-T. Wang, H.-S. Sheu and W.-F. Hsieh, J. Phys.: Condens. Matter, 2007, 19, 476212.
- 21 Y.-W. Ju, J.-H. Park, H.-R. Jung, S.-J. Cho and W.-J. Lee, *Materials Science and Engineering B*, 2008, **147**, 7–12.
- 22 D. Chien, A. N. Buditama, L. T. Schelhas, H. Y. Kang, S. Robbennolt, J. P. Chang and S. H. Tolbert, *Appl. Phys. Lett.*, 2016, 109, 112904.
- 23 V. M. Petrov, J. Zhang, H. Qu, P. Zhou, T. Zhang and G. Srinivasan, J. Phys. D: Appl. Phys., 2018, 51, 284004.
- 24 C. S. Smith, R. Bowrothu, Y. Wang, F. Herrault, Y. K. Yoon and D. P. Arnold, *IEEE Trans. Magn.*, 2021, 57, 1–5.
- 25 F. Li, T. Wang, L. Ren and J. Sun, *J. Phys.: Condens. Matter*, 2004, **16**. 8053–8060.
- 26 J. De La Torre Medina, M. Darques, L. Piraux and A. Encinas, *Journal of Applied Physics*, 2009, **105**, 023909.
- 27 V. Vega, T. Böhnert, S. Martens, M. Waleczek, J. M. Montero-Moreno, D. Görlitz, V. M. Prida and K. Nielsch, *Nanotechnology*, 2012, 23, 465709.
- 28 B. D. Culity and C. D. Graham, *Introduction to Mangetic Materials*, IEEE, Hoboken, New Jersey, 2nd edn., 2009.

Page 5 of 5 ChemComm

The data underlying this study are available in the published article and its electronic supplementary information (ESI).